Photothermal flash light doping of strontium titanate photocatalyst nanoparticles

Supplementary information (SI)

Melanie Johanning[1], Wanderson Oliveira da Silva[2], Anselm Dreher[3], Paul Kant[3], Mara Blöchlinger[1], Arthur E. Bouchez[1], Coral Felipe Gracia[4], Hannah Johnson[4], Roland Dittmeyer[3], Mathieu Soutrenon[2], Kevin Sivula[1]

[1] Laboratory for Molecular Engineering of Optoelectronic Nanomaterials (LIMNO), Institute of Chemical Sciences and Engineering, EPFL, Lausanne CH-1015, Switzerland

[2] Institute of Systems Engineering, HES-SO Valais- Wallis, Sion CH-1950, Switzerland

[3] Institute for Micro Process Engineering (IMVT), Karlsruhe Institute of Technology (KIT), 76344 Eggenstein-Leopoldshafen, Germany

[4] Materials Engineering, Toyota Motor Europe, 1930 Zaventem, Belgium

Section 1: Methods

1.1 Synthesis

The synthesis workflow to compare flash light annealing (FLA) and thermal annealing (TA) is shown in Figure 1 of the main text. Commercial $SrTiO_3$ (Iolitec, 100 nm, 99.9%) was impregnated with Rh and La precursors by manual wet grinding. Dopant salts for 1 at.% Rh ([Rh] = [Rh]/[Rh]+[Ti]) from $RhCl_3 \cdot H_2O$ (Sigma Aldrich, 38-40% Rh)) and 1 at.% La ([La] = [La]/[La]+[Sr] assuming [Sr] = [Ti] from $La(NO_3)_3 \cdot 6H_2O$ (IVALUA, +98 %)) were mixed with the powder and 2 mL ultrapure (UP) water (18 MΩ) in an agate mortar. The mixture was ground for 10 min followed by continuous grinding during evaporation on a hot plate at 150 °C. The precursor was dried at 80 °C for 12 h under vacuum.

The pristine commercial powder and impregnated powder were dispersed (40 mg mL^{-1}) in isopropanol (Fisher Scientific, >99.8 %) by bath sonication for 60 min with regular shaking. Silicon substrates cleaved from wafers (~2 cm x 2.5 cm, University wafers, <100>, grade virgin test, thickness 500 ± 25 µm) were prepared for coating by 15 min treatment in a UV ozone cleaner. The wafers were drop coated with a loading of 0.08 mL cm^{-2} of the dispersion at room temperature.

FLA experiments comparing doped and undoped samples were conducted using a Xenon flash lamp (Flexe 3 NFS2016 16 kW, Excelitas NobleLight, England). A quartz block of 25 x 20 x 107 mm^3 (length x width x height) placed below the flash lamp served as a light guide and for protection. The silicon substrates were placed on thermally insulating, porous Al_2O_3/SiO_2 (Schupp, UltraBoard, thickness 2 mm) on a stainless-steel support. The distance of the sample to the quartz light guide was 35.4 mm. Two samples were annealed simultaneously at each condition to produce enough powder. The frequency and pulse width were fixed at 60 Hz and 1.5 ms, respectively, for all experiments. The effect of the voltage and number of pulses was tested. In one series, 250 V were used with 450, 900, 1800, 3600, and 7200 pulses. In a second series, the voltage was varied as 225 V, 250 V, and 275 V with 1800 pulses. An additional sample was annealed using 450 pulses at 275 V. The two best photocatalytic performances were achieved with 1800 pulses at 250 V and 450 pulses at 275 V.

The overview of conditions, power, and energy consumption of the flash lamp is listed in Table S1. It can be assumed that only around 50 % of the consumed energy is emitted in the form of light. The calculations were based on the "Hereaus Noblelight technical reference book for arc and flash lamps".[1] The pulse power PP was calculated based on the lamp's impedance constant K_0 and current I:

$$PP = K_0 \, I^{3/2} \tag{1}$$

Here, I was determined using equation (2) with the pulse width T and the energy E_0 stored in the capacitor. E_0 was calculated using equation (3) based on the capacitance C and the initial voltage across the capacitor V_0, i.e., the set voltage.

$$I = \left(\frac{E_0}{K_0 T}\right)^{2/3} \tag{2}$$

$$E_0 = \frac{C \, V_0^2}{2} \tag{3}$$

The average power AP was calculated from the pulse power PP using equation (4), where f is the pulse frequency. The total energy consumption E was obtained from equation (5), where n is the number of pulses.

$$AP = PP \cdot T \cdot f \tag{4}$$

$$E = AP \cdot f \cdot n \tag{5}$$

The annealed powder was collected from the silicon substrates by brief bath sonication in UP water. After the powder has resettled, the water was carefully removed with a pipet. The powders were dried at 80 °C for 12 h under vacuum. Direct FLA of the precursor powder was performed on silicon, quartz glass (Edmund Optics, diameter 20 mm, thickness 2 mm), and Al_2O_3 (crucible lid, thickness 3.5 mm, diameter 50 mm). A few mg were spread on the substrate and collected after flashing.

Thermal reference samples were synthesized at 1100 °C for different annealing times with and without a heating ramp. For a conventional doping, the impregnated precursor was annealed at 1100 °C for 6 h in an Al_2O_3 boat with a ramp time of 3.6 h and allowed to cool down naturally.[2] For short-time thermal annealing without a conventional heating ramp, the coated silicon on the Al_2O_3/SiO_2 plate or powder in an Al_2O_3 boat were slid into a pre-heated tube furnace at 1100 °C. After annealing for 10 min and 30 min, the samples were taken out to ambient temperature immediately. Another reference using this approach was annealed at 800 °C for 120 min.

The undoped hydrothermal cubes used as a precursor were synthesized based on a procedure reported elsewhere.[3] 0.937 mL of 2.5 M $TiCl_4$-solution in UP water (Thermo Scientific Acros, 99.9 %) was dropped into a mixture of 21.5 mL UP water and 2.54 mL methanol stirred in an ice bath. The flask was closed, connected to a Schlenk line and placed under Argon atmosphere to reduce formation of $SrCO_3$.[4] The solution was purged initially and the needle then placed above the solution. 40 mL of LiOH solution (1.787 M, LiOH ·H_2O, Thermo Scientific Alfa Aesar, 99.995 %) were added dropwise and the reactor was stirred for another 30 min. Next, 10 mL of $SrCl_2$-solution (0.263 M, $SrCl_2 \cdot 6H_2O$, Thermo Scientific Alfa Aesar, 99-103 %) were added dropwise and the mixture stirred for another 30 min. The solution was filled into a 100 mL Teflon-lined autoclave, degassed with N_2, and heated at 180 °C for 48 h (Memmert, UF 30 plus). The obtained powder was washed three times in UP water and three times in ethanol by sonication and centrifugation. The final sample was dried at 80 °C for 12 h under vacuum.

1.2 Characterization

The crystal structure and phase purity of the powders were examined by X-ray powder diffraction (XRD) in Bragg-Brentano geometry (Bruker, D8 Discover Vario) using $CuK_{\alpha 1}$ radiation. Reference patterns were obtained from the COD data base [5–13] and plotted by Vesta (Version 3.5.8, JP-Minerals). For scanning electron microscopy (SEM), the samples were coated with 6 nm Ir as conductive coating and then observed in a Zeiss Merlin microscope at 0.8 kV. Scanning transmission electron microscopy with energy-dispersive X-ray spectroscopy (STEM-EDX) mapping was performed at 200 kV in a Tecnai Osiris equipped with four Super-X EDX SDD detectors. The elemental maps were analyzed by Velox Software (Thermo Fisher Scientific, v3.12.0). STEM images of selected samples were acquired for particle size analysis. At least 200 particles were counted manually per sample using ImageJ v. 1.54p. Sintered (i.e., fused) particles were counted as one particle and measured along their longest dimension, if the sintering was clearly visible. Otherwise, particles were counted separately. However, due to the 2D projection in TEM, a clear distinction between sintered and overlapping particles was not always possible. The STEM images along with the marked images for counted particles are provided in the supporting data repository. The analysis of crystallinity by TEM through convergent beam electron diffraction (CBED) and high-resolution TEM (HRTEM) was performed on a Talos F200S at 200 kV. The CBED patterns were indexed using CrysTBox.[14–16]

X-ray photoelectron spectroscopy (XPS) measurements were carried out to analyze the surface concentration of the dopants for selected samples. Measurements were performed on an Axis Supra (Kratos Analytical) using the monochromated K_α X-ray line of an Aluminum anode. The pass energy was set to 40 eV with a step size of 0.15 eV. The samples were pressed onto an Indium foil. Nevertheless, some charging occurred, and the best results were obtained by using a low energy electron flood to neutralize the charge buildup. Data processing was done with CasaXPS and started by energy referencing the data at 284.8 eV with the CC, CH component of the C 1s line. The measurement of bulk elemental concentrations and test for silicon impurities was performed by inductively coupled plasma mass spectroscopy (ICP-MS) using an Agilent 8900 Triple Quadrupole instrument. The powder samples were digested in aqua regia by 30 min ultrasonication and subsequently centrifuged to remove any solid residues before taking the supernatant for dilution and subsequent analysis. The particle size measurements by dynamic light scattering (DLS) were carried out on particle dispersions (0.1 mg mL^{-1} in UP water) in plastic cuvettes (ZEN0040) using a Zetasizer Pro blue label instrument (Malvern Panalytical). The laser wavelength was 632.8 nm and the scattered signal was measured at an angle of 173°. To calculate the particle size distribution by number using the Z average, the refractive index of 2.41 was assumed.

<u>Ray tracing model for optical properties</u>

Absorption and scattering coefficients of catalyst dispersions were derived from UV-Vis total (= hemispherical) reflection and transmission measurements employing the methodology for the determination of absorption and scattering coefficients of turbid volumes published by Kant et al. elsewhere.[17]

The measurements of total reflection and transmission of the powder dispersions in a quartz cuvette (pathlength 10 mm) were conducted using a Shimadzu UV-3600 equipped with an integrating sphere. The powder dispersions were prepared as for photocatalytic tests (0.5 mg mL^{-1} in UP water). Each reflection and transmission measurement was performed in the band from 300 nm to 800 nm with a resolution of 1 nm. Each measurement was repeated three times. The cuvette was shaken between all measurements to prevent sedimentation. A $BaSO_4$ standard referenced to a PTB-referenced

Spectralon 99% reflection standard (Sphere Optics, SG3052, serial number 21RW0203) was used for correcting the relative reflection measurements and calculate the absolute reflection.

Briefly summarizing, the total reflection and transmission data obtained in the UV-Vis experiments was evaluated using a 3D optical model of the UV-Vis cuvette. The optical model of the UV-Vis cuvette was set up in a MATLAB®-based ray tracing environment published elsewhere[18] and described in detail elsewhere.[19] In the optical model, the UV-Vis cuvette was approximated as a tube with a rectangular cross-section and constant wall thickness of 1.22 mm filled with a rectangular block of catalyst dispersion. The geometric dimensions equaled those experimentally determined from the actual UV-Vis cuvette. For clarification of the assumed geometry, see Figure S4a.

The refractive index and absorption coefficient of quartz glass assumed in the simulation were taken from literature.[20] The refractive index of the catalyst dispersion in the simulation was assumed to be identical with that of pure water and taken from literature.[21] The absorption and scattering coefficient of the catalyst dispersion were varied in the simulations in steps of 10 m^{-1} in the range from 0 m^{-1} to 2000 m^{-1} to obtain an "optical behavior map" of the UV-Vis cuvette (see Figure S4 (b)). The map tells which total reflection and transmission can be expected from the UV-Vis cell for a given set of absorption and scattering coefficient of the catalyst dispersion mapped in the simulations. By fitting experimental data pairs of reflection and transmission to the map data with a least square estimator, absorptions and scattering coefficients of actual dispersions were finally determined.

Photocatalytic screening test

The photocatalytic performance was tested using purged-type reactors at ambient pressure connected to an on-line gas chromatograph (Shimadzu Nexis GC-2030). For screening tests, 3 mL glass vials purged with nitrogen (N_2) at 1 mL min^{-1} were used as the reactor. Four vials were measured simultaneously using a selector valve (Vici flow-through 8-port selector valve) coupled to the GC software LabSolutions by LabVIEW (2022 Q3). Data analysis was performed using a modular, browser-based electronic lab notebook.[22,23] The powder dispersions were illuminated from the bottom while stirring continuously with 8 mm x 1.5 mm stir bars.

Tests were performed for sacrificial hydrogen (H_2) evolution from aqueous dispersions with ascorbic acid as a sacrificial agent (0.2 M, Sigma Aldrich) using 0.4 wt.% Pt (K_2PtCl_6, abcr GmbH, 99%) as the co-catalyst. The powders were dispersed in UP water (0.5 $mgmL^{-1}$) using a mortar and bath sonication. Appropriate amounts of ascorbic acid and Pt precursor solution (1 $mgmL^{-1}$) were added to the reactor vials. The samples were degassed before performing in-situ photodeposition for 30 min under 365 nm LED illumination at 12 mW cm^{-2} (Thorlabs M365LP1 with collimator SM1U25-A). The performance was subsequently measured at 365 nm (3.56 mW cm^{-2}) and 415 nm (3.14 mW cm^{-2}, Thorlabs M415LP1 with collimator SM2F32-A). The light spectra of both LEDs are shown in Figure S17a. The measurements were performed until the H_2 production rate stabilized for at least three measurements of each vial to calculate an average performance for each wavelength. At least two measurements were performed per sample and the average performance value was calculated.

For measurements under simulated sunlight, the samples were placed above a mirror reflecting light emitted from a 450 W Xenon arc-lamp behind a KG2 filter. A 420 nm cut-off filter was placed inside the light path shortly before the end of the run. The respective spectral shapes with and without the cut-off filter are shown in Figure S17b.

Apparent quantum yield measurements

The apparent quantum yield (AQY) was measured for one sample as a bench mark. A 40 mL top-illuminated reactor purged with N_2 at 10 mLmin^{-1} and equipped with a quartz window was used for this measurement. 10 mg of sample were dispersed in 40 mL of 0.2 M ascorbic acid solution. 0.4 wt.% Pt were deposited by photodeposition for 30 min at 16 mW cm^{-2}. The same illumination conditions as above were used to measure the steady state H_2 production rates at 365 and 415 nm. The AQY was calculated using equation (6):

$$AQY\ (\%) = \frac{n_e}{n_{ph}} \cdot 100 \tag{6}$$

Here, n_e is the number of reacted electrons per second and n_{ph} the number of incident photons per second. These quantities were calculated using equations (7) and (8) from the H_2 production rate r_{H2} in µmols^{-1}, the Avogadro constant N_A, the irradiance I, illumination area A (3.01 cm^2 for 365 nm and 2.35 cm^2 for 415 nm), the Planck's constant h, the speed of light c, and the wavelength λ.

$$n_e = r_{H2} \cdot N_A \cdot 2 \tag{7}$$

$$n_{ph} = \frac{I \cdot A}{h \cdot \frac{c}{\lambda}} \tag{8}$$

Calculation of the solar-to-hydrogen (STH) efficiency

The STH efficiency was calculated under consideration of the spectral mismatch of the simulated solar light emitted by the Xe lamp and the nominal spectrum of AM 1.5G sunlight according to equation (4):

$$\boldsymbol{STH}\ (\%) = \frac{r_{H2} \cdot \Delta G(H_2)}{I_{1sun} \cdot A \cdot x_{sun}} \cdot 100 \tag{9}$$

Here, $\Delta G(H_2)$ the reaction Gibbs energy of water splitting, I_{1sun} the nominal irradiance of 100 mW cm^{-2} of sunlight, A the illumination area (1.43 cm^2) and x_{sun} the share of 1 sun illumination considering the spectral mismatch. x_{sun} was determined as the share of photons absorbed by a material with band gap of 3.2 eV (undoped precursor) and 2.5 eV (1 % Rh,La FLA) in the measurement conditions as compared to AM 1.5G illumination.

Section 2: Supplementary figures

Conservation of initial powder morphology during impregnation by wet grinding

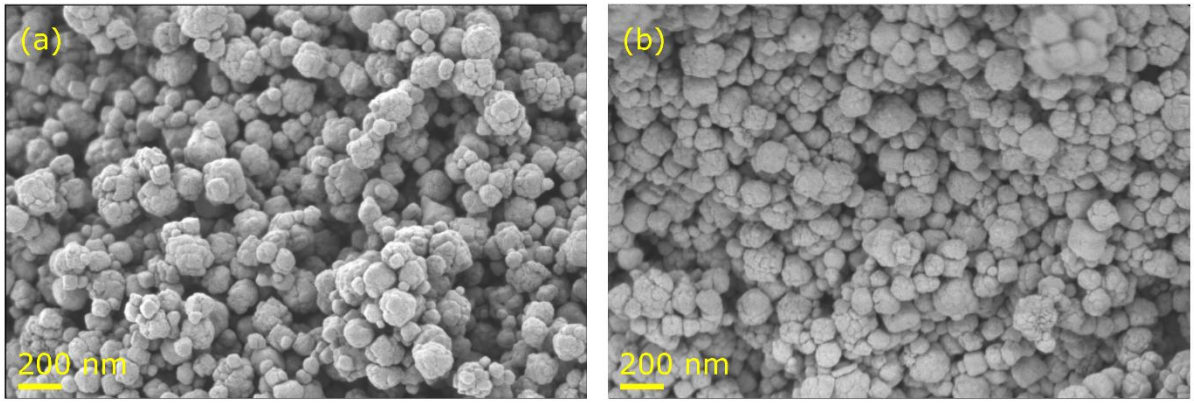

Figure S1: SEM images comparing the powder morphology of (a) the pristine precursor and (b) the powder impregnated with 1 % Rh and La by wet grinding.

Homogeneity of the product from FLA for the chosen film thickness

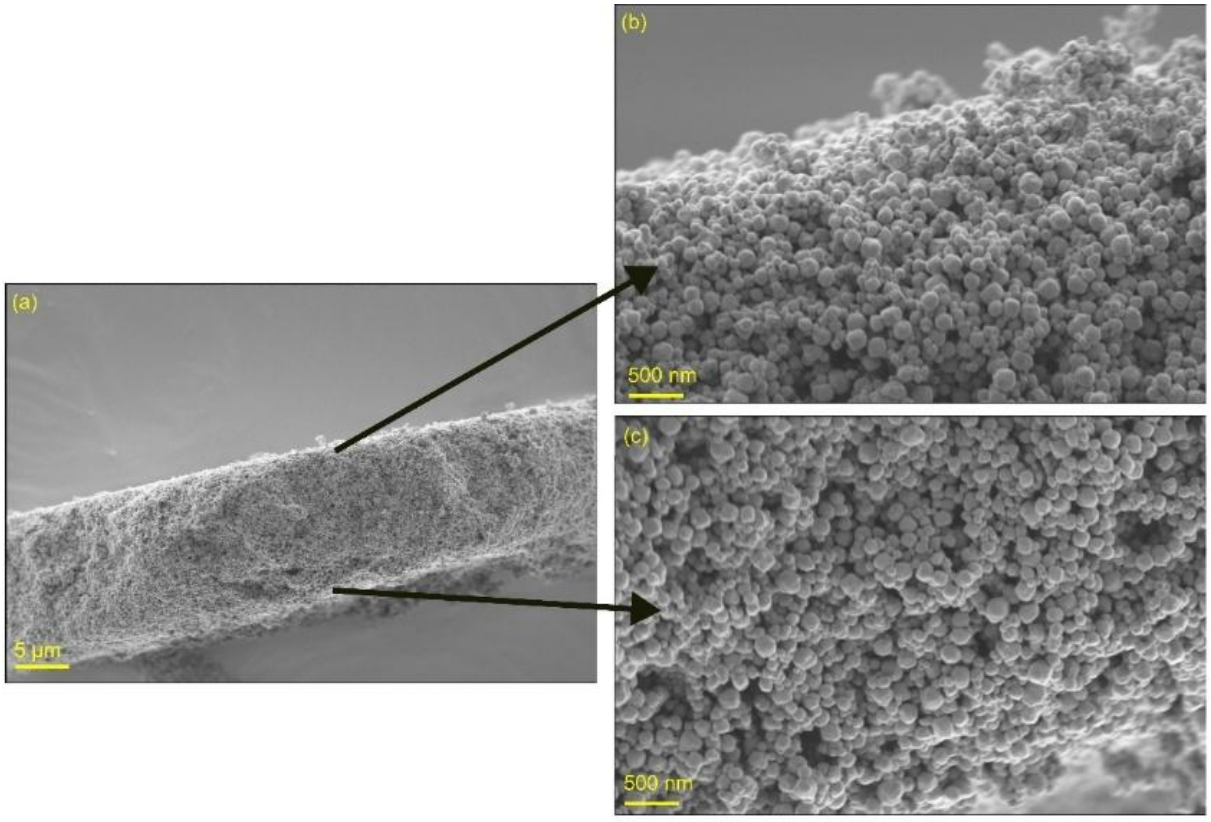

Figure S2: SEM images showing (a) a flake of Rh,La:$SrTiO_3$ in side view after doping by FLA at 250 V and 1800 pulses with a homogeneous transformation of the (b) top and (c) bottom side.

Photographs of thermal references and undoped references

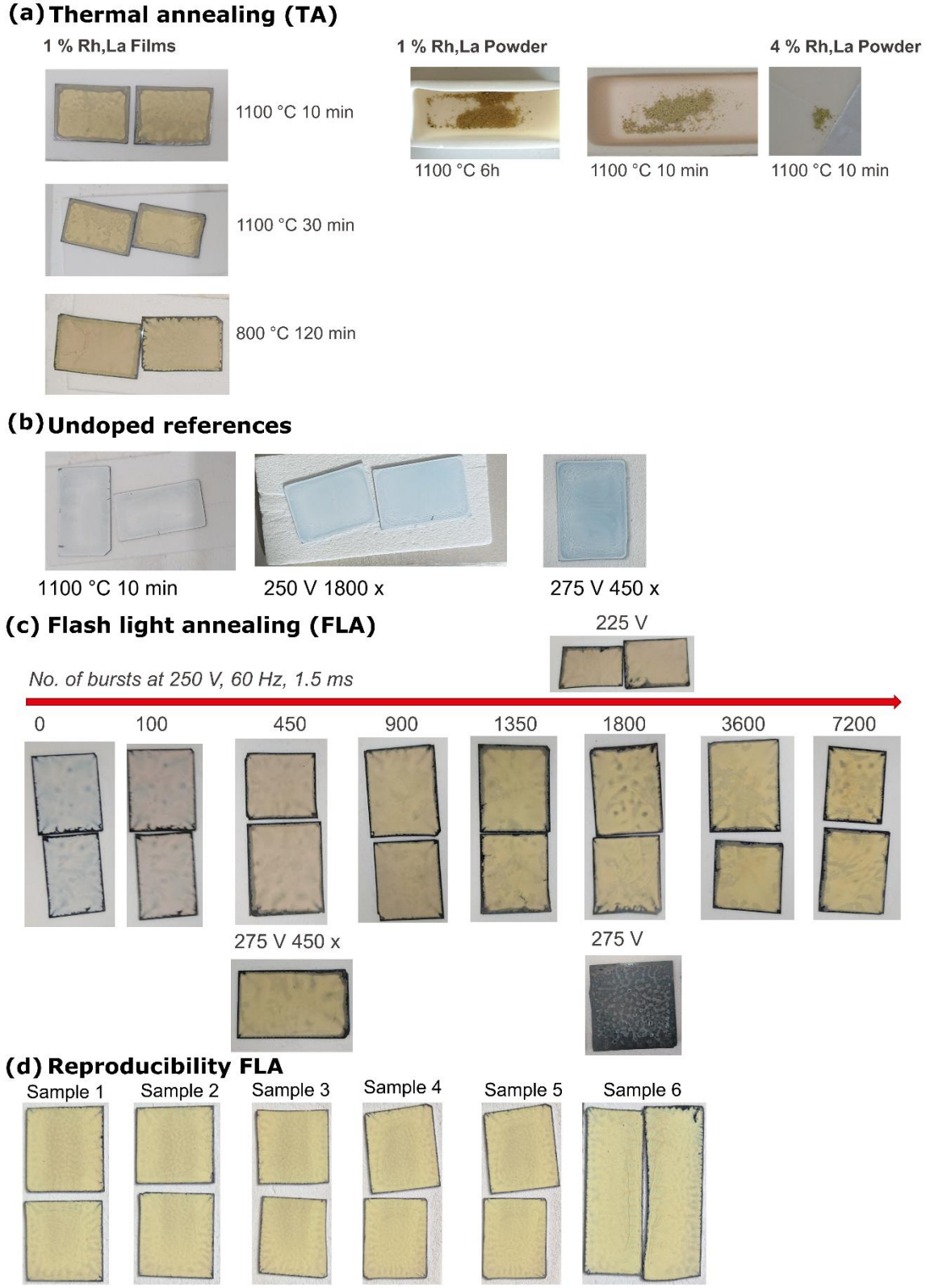

Figure S3: Photographs of all samples (a) doped with thermal annealing (TA) coated on Si substrates and as free powder, (b) undoped references from FLA, (c) doped with flash light annealing (FLA) at different voltages and number of pulses, and (d) doped via FLA at 250 V and 1800 pulses to test the reproducibility of the FLA technique.

Simulation domain and optical behavior map used to determine optical properties of dispersions

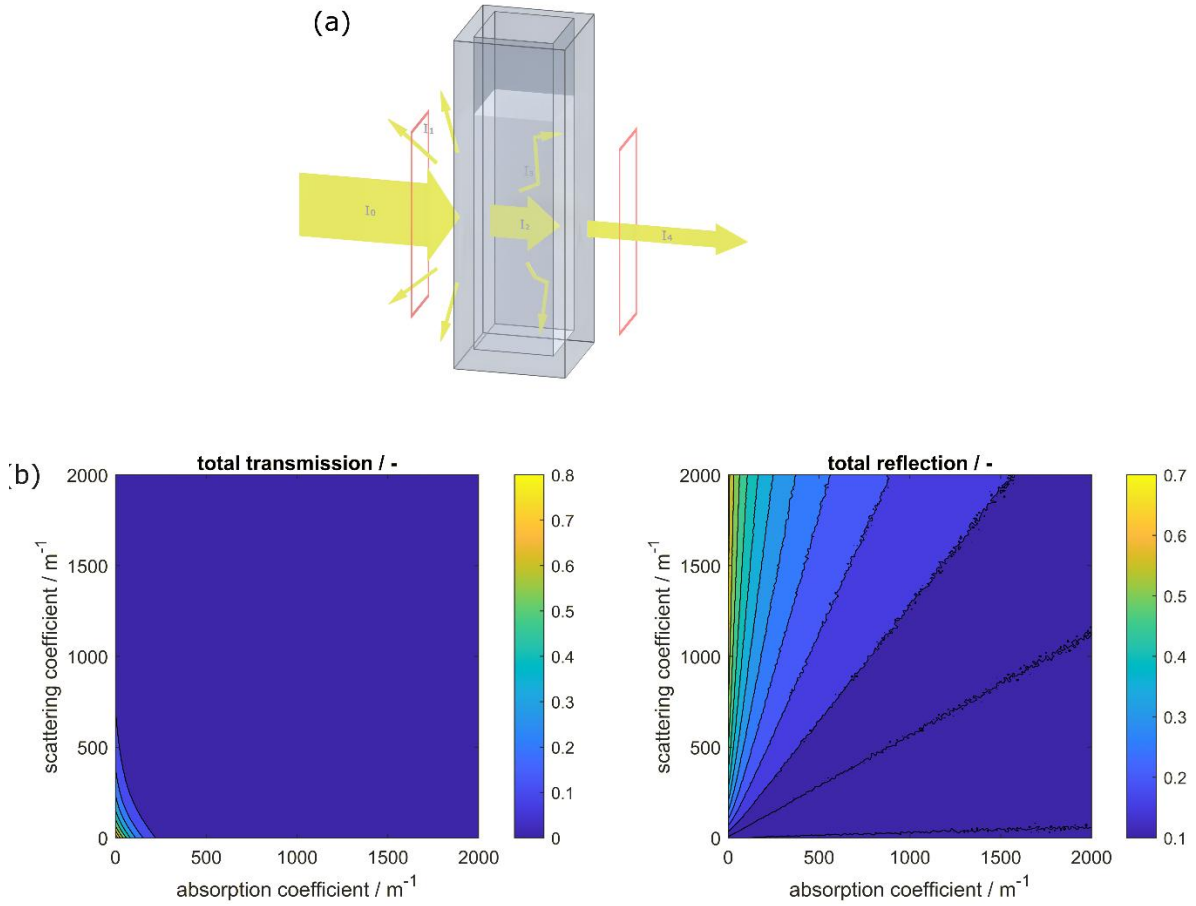

Figure S4: (a) Simulation domain approximating the UV-Vis cuvette in the optical simulations underlying the data evaluation delivering absorption and scattering coefficients from UV-Vis total reflection and transmission measurements. This is achieved by modelling the spectrometers light beam (I_0), its total reflection at the catalyst suspensions surface (I_1), the attenuation (I_2), the volumetric scattering (I_3) inside the suspension, and the transmission (I_4). Partial reflections on the phase boundaries are considered but not shown here. The red rectangles represent the layers on which rays for total reflection and transmission are counted. (b) Simulated "optical behavior map" of the UV-Vis cuvette showing the reflection and transmission data obtained in simulations for any set of absorption and scattering coefficient in the range from 0 m^{-1} to 2000 m^{-1}.

Extended data belonging to optical absorption coefficients in Figure 2 and reference of Kubelka-Munk function measured by diffuse reflectance of powders

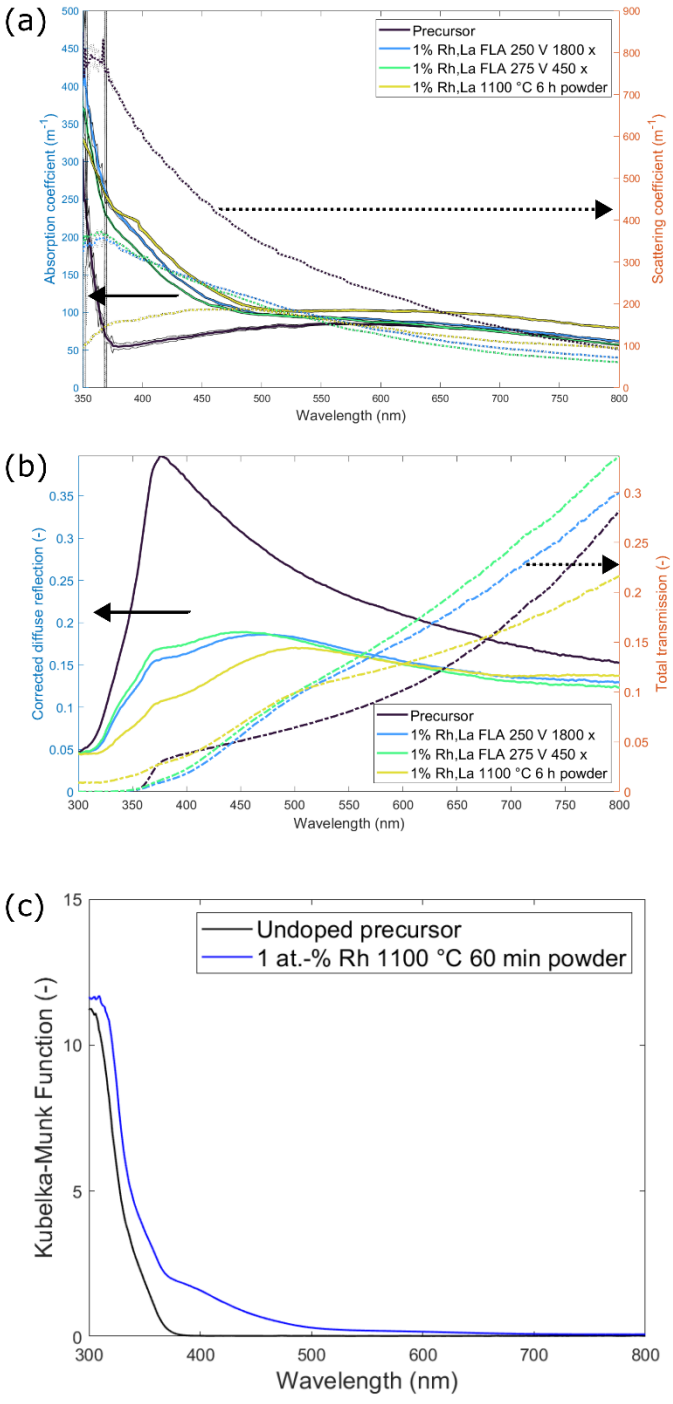

Figure S5: (a) Scattering coefficients (dashed lines) along with absorption coefficients (solid lines) for samples in Figure 2c in the main text plotted together with their respective standard deviation. The conditions were chosen for a good resolution of the visible light absorption feature. Absorption of photons with energy exceeding the band gap of undoped $SrTiO_3$ was too strong to allow transmission through the cuvette. Total transmission approaches zero below 370 nm with the absorption onset of undoped $SrTiO_3$ (see (b)). Therefore, the optical absorption and scattering coefficients cannot be extracted accurately enough below 350 nm as the least square estimator does not converge to a unique value pair. (b) Diffuse reflection and transmission data used for the extraction of optical properties of Figure S5a and Figure 2c. (c) Example of calculated Kubelka-Munk function from total reflection measurements of pressed powders comparing the undoped precursor compared to 1 % Rh,La:$SrTiO_3$ doped by thermal annealing at 1100 °C for 60 min.

XRD Patterns

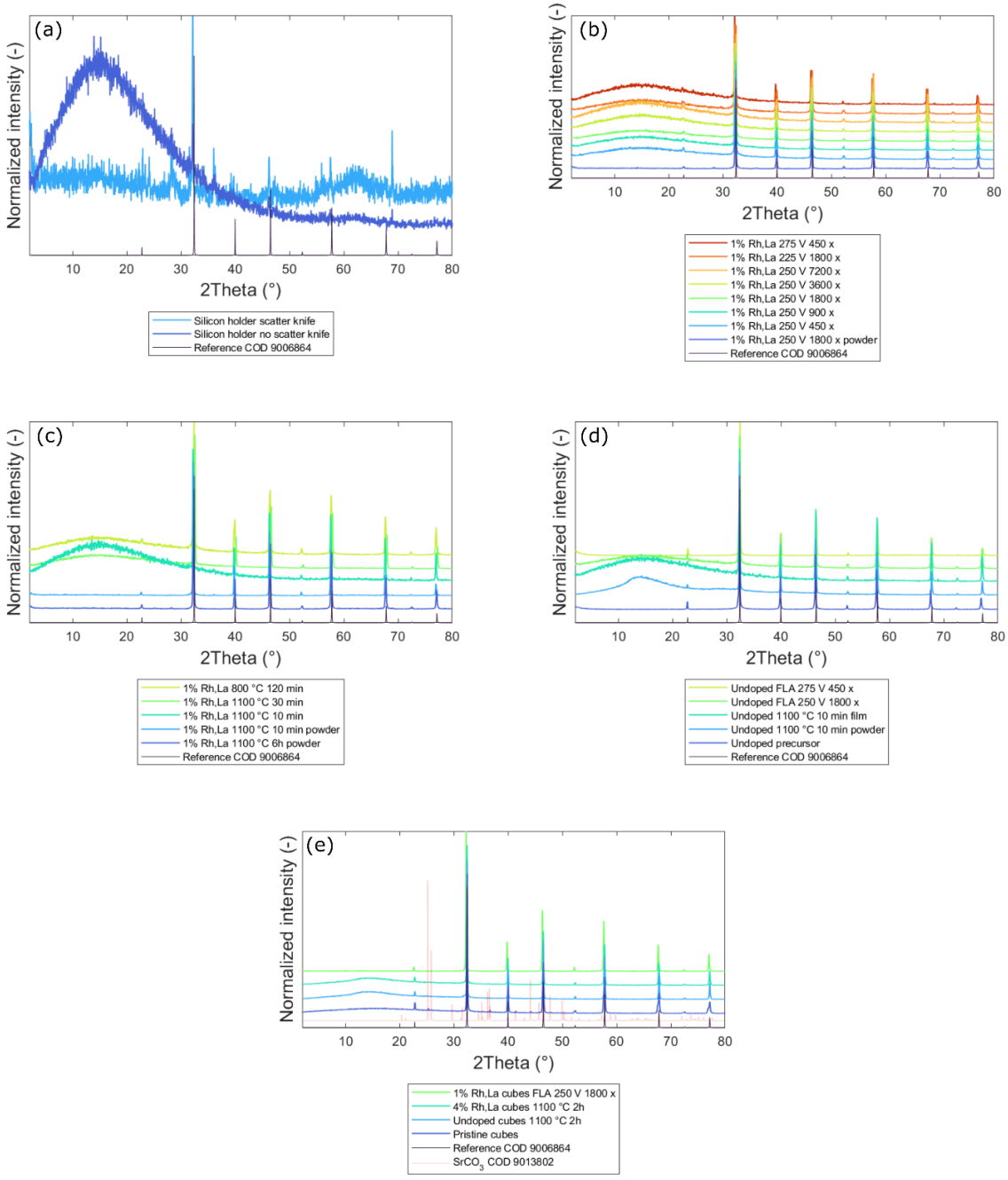

Figure S6: Powder XRD patterns of different samples along with empty sample holders. (a) Empty silicon sample holders with and without employing a scattering knife along with a reference pattern for cubic $SrTiO_3$ from the COD data base[5–13] simulated by Vesta. Due to imperfections in the silicon sample holders, small diffraction peaks are visible for the empty holder. Some of the peaks overlap with the $SrTiO_3$ diffraction pattern. The remaining peaks are responsible for the slightly visible additional peaks in the XRD patterns. The sample holder diffraction patterns changed over time and vary between sample holders; hence the visibility of impurities varies between different samples. The amorphous background intensity is sensitive to the position of the scatter knife and the amount of sample measured. This causes variations in the background intensities for the XRD data of different samples. Normalized powder XRD patterns of (b) 1 % Rh,La:$SrTiO_3$ doped with FLA, (c) 1 % Rh,La:$SrTiO_3$ doped with TA, (d) undoped reference samples, and (e) pristine as well as 1% Rh,La-doped cubes synthesized with the hydrothermal method along with reference pattern for cubic $SrTiO_3$ from the COD data base.[5–13] An additional reference pattern for $SrCO_3$ impurities is shown in (e). The impurities disappear upon annealing at 1100 °C for 2h, even for the bare sample without addition of dopants.

SEM comparing FLA and TA samples annealed at different conditions

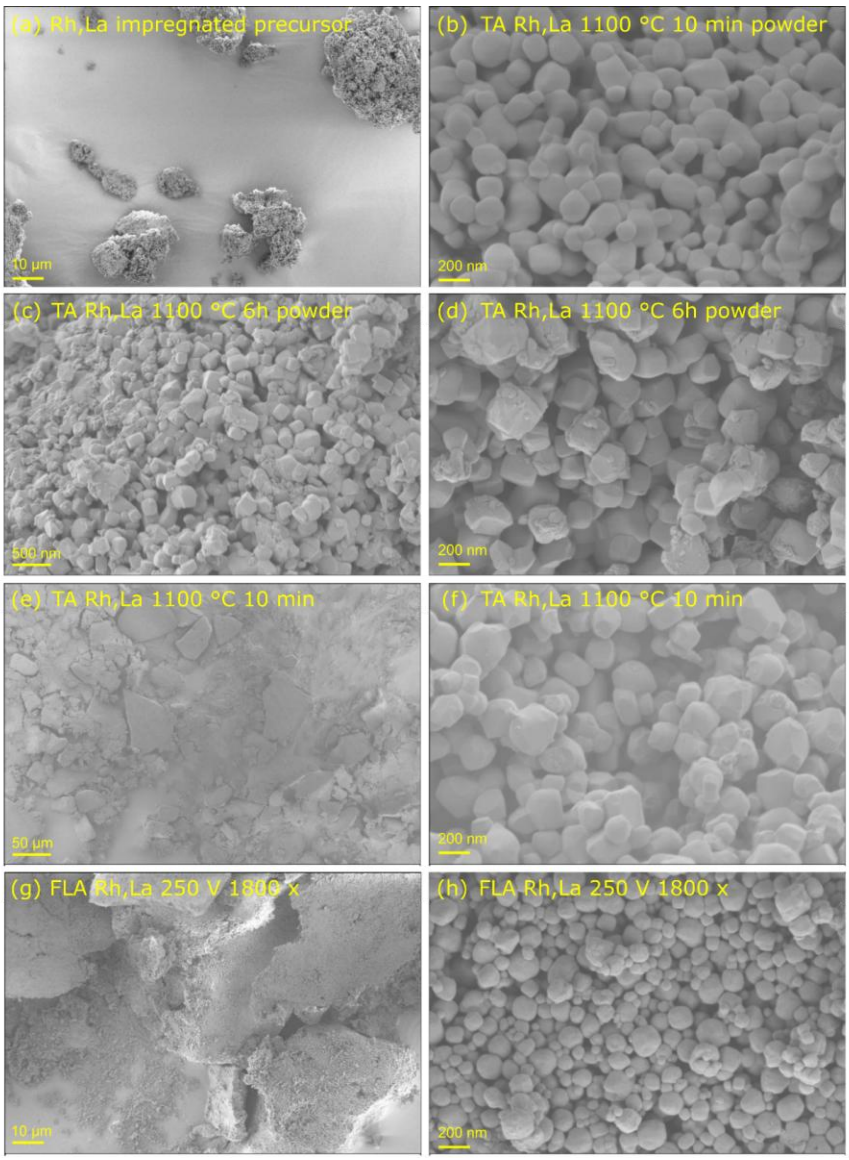

Figure S7: SEM images of 1 % Rh,La samples. (a) Powder aggregates present in the precursor, which sinter upon annealing to different degrees depending on the annealing conditions. SEM images of samples doped with thermal annealing (TA) as (b) powder for 10 min, (c-d) 6 h, and (e-f) as a film for 10 min and (g-h) with two FLA conditions. The samples from TA sintered significantly more than after FLA. FLA and TA samples doped on silicon substrate both form larger plate-like aggregates, but aggregates of the TA sample are connected stronger through sintering and the particle surface restructured more (see e-h).

Undoped reference samples

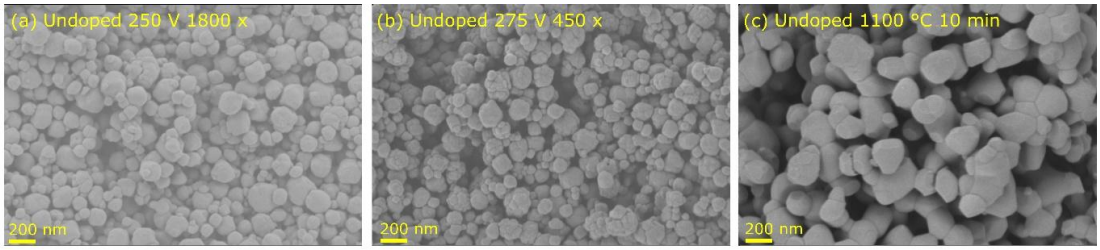

Figure S8: SEM images of undoped samples after (a) FLA at 250 V and 1800 pulses, (b) 275 V and 450 pulses and (c) TA at 1100 °C for 10 min.

Heating ramp upon exposure to 1100 °C in an Al_2O_3 tube

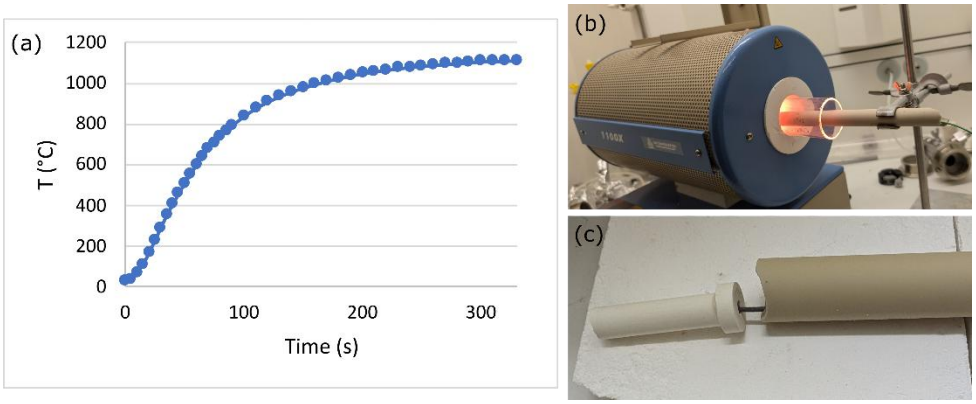

Figure S9: (a) Temperature vs. time profile for a K-type thermocouple in an Al_2O_3 tube when exposed to the pre-heated tube furnace at 1100 °C as used for TA of samples between 10 and 120 min. The measurement set-up is shown in (b) and (c).

STEM-EDX mapping for 1 % doping by FLA and TA

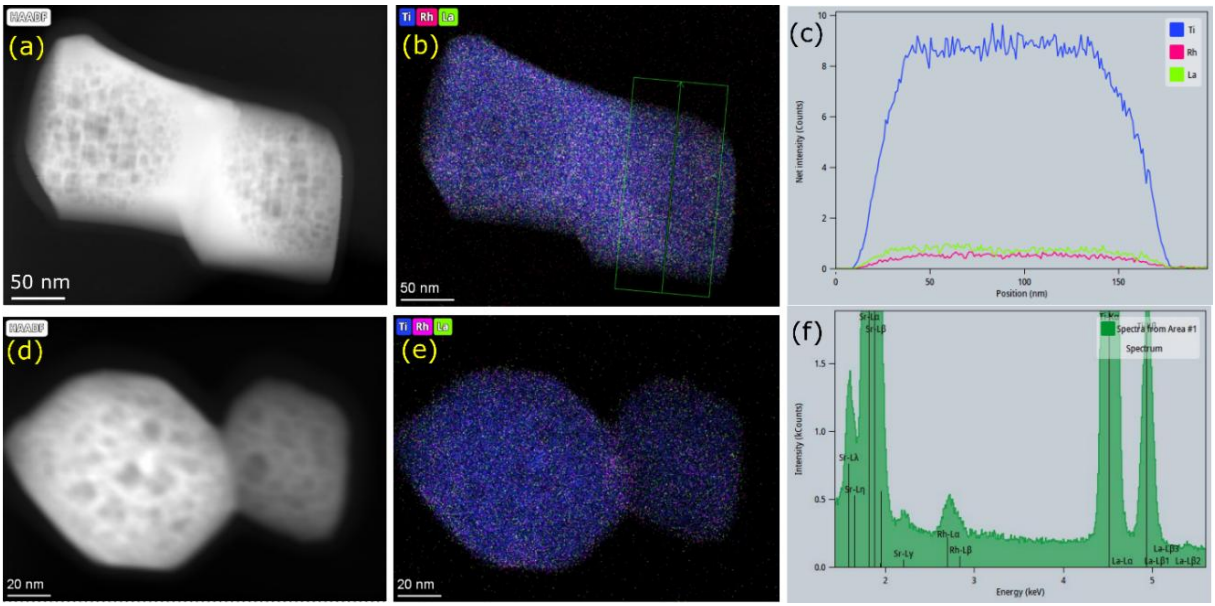

Figure S10: STEM-EDX mapping for samples with 1 % Rh,La-doping. (a-c) HAADF signal, elemental map of net counts, and corresponding line profile for a sample doped by TA at 1100 °C for 6 h. The dopant concentration is too low to detect a core/shell structure. The internal structure with voids remains intact. However, a certain fraction between the particles was reformed without voids by sintering (bulk part between the two particles). (d-e) HAADF signal and elemental maps of net counts for FLA (250 V, 1800 x). The dopant distribution is not visible, either. Only a small fraction of the particle at the surface restructured. (f) The EDX spectrum of the FLA sample shows the presence of Rh and La. La peaks overlap with Ti peaks but can be deconvoluted using the La-$L_{\beta 2}$ peak.

STEM-EDX mapping for 4 at.% Rh,La doping by TA for 10 min at 1100 °C

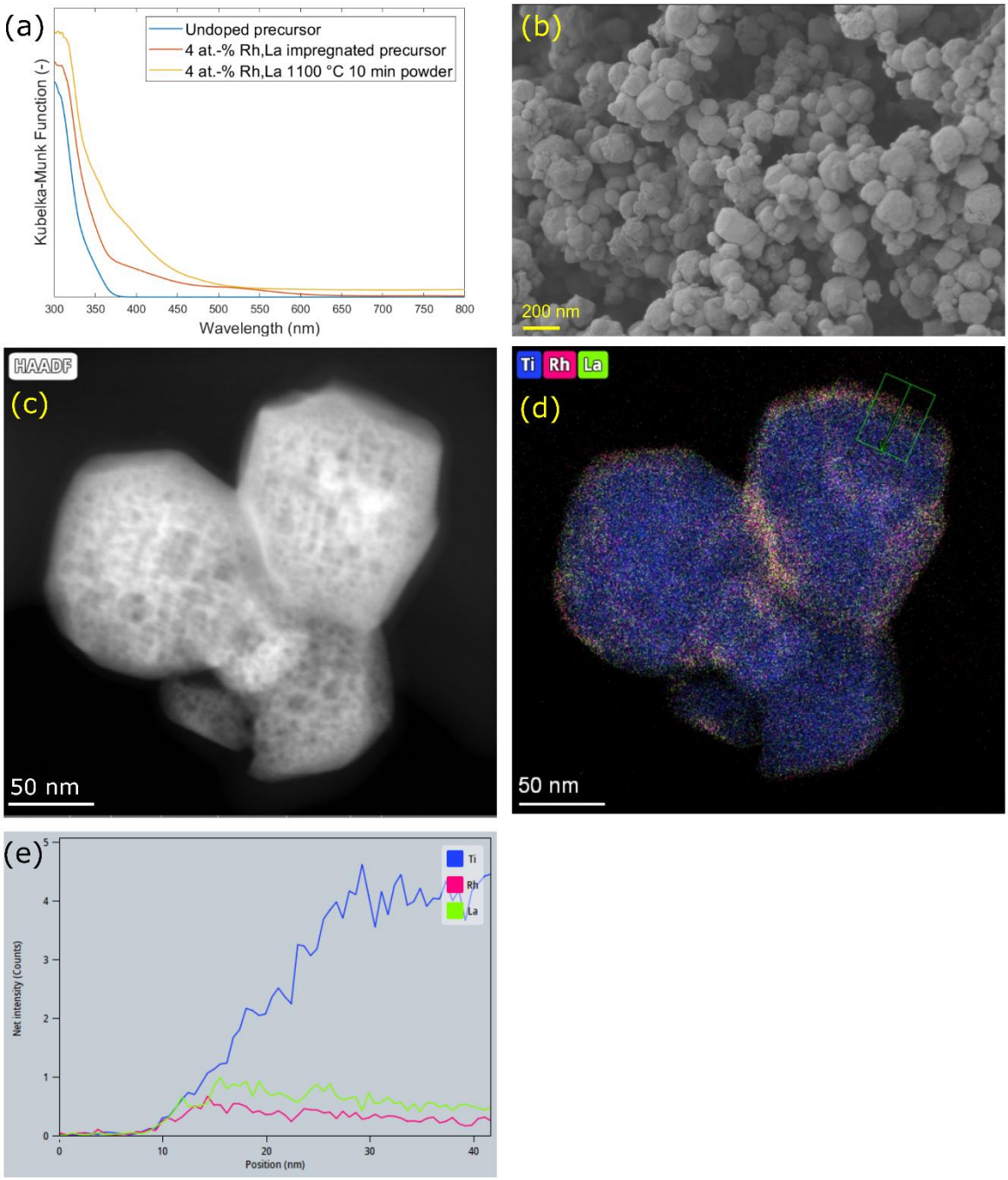

Figure S11: (a) Kubelka-Munk function of 4 % Rh,La:$SrTiO_3$ annealed for 10 min in a pre-heated tube furnace features a similar absorption onset at 500 nm and increased absorption compared to the undoped and salt-impregnated precursors. (b) SEM image of 4 % Rh,La-doped $SrTiO_3$ after 10 min TA shows the presence surface restructuring as for 1 % doping. (c) STEM-EDX HAADF signal for for 4 % Rh,La:$SrTiO_3$ after 10 min thermal annealing along with (d) an elemental map of net counts and (e) the line profile for the trace marked in (d). The images reveal the formation of a core/shell structure. The internal particle structure with voids is conserved and the dopants are incorporated into the restructured shell.

XPS spectra and 2nd data set of dopant concentrations

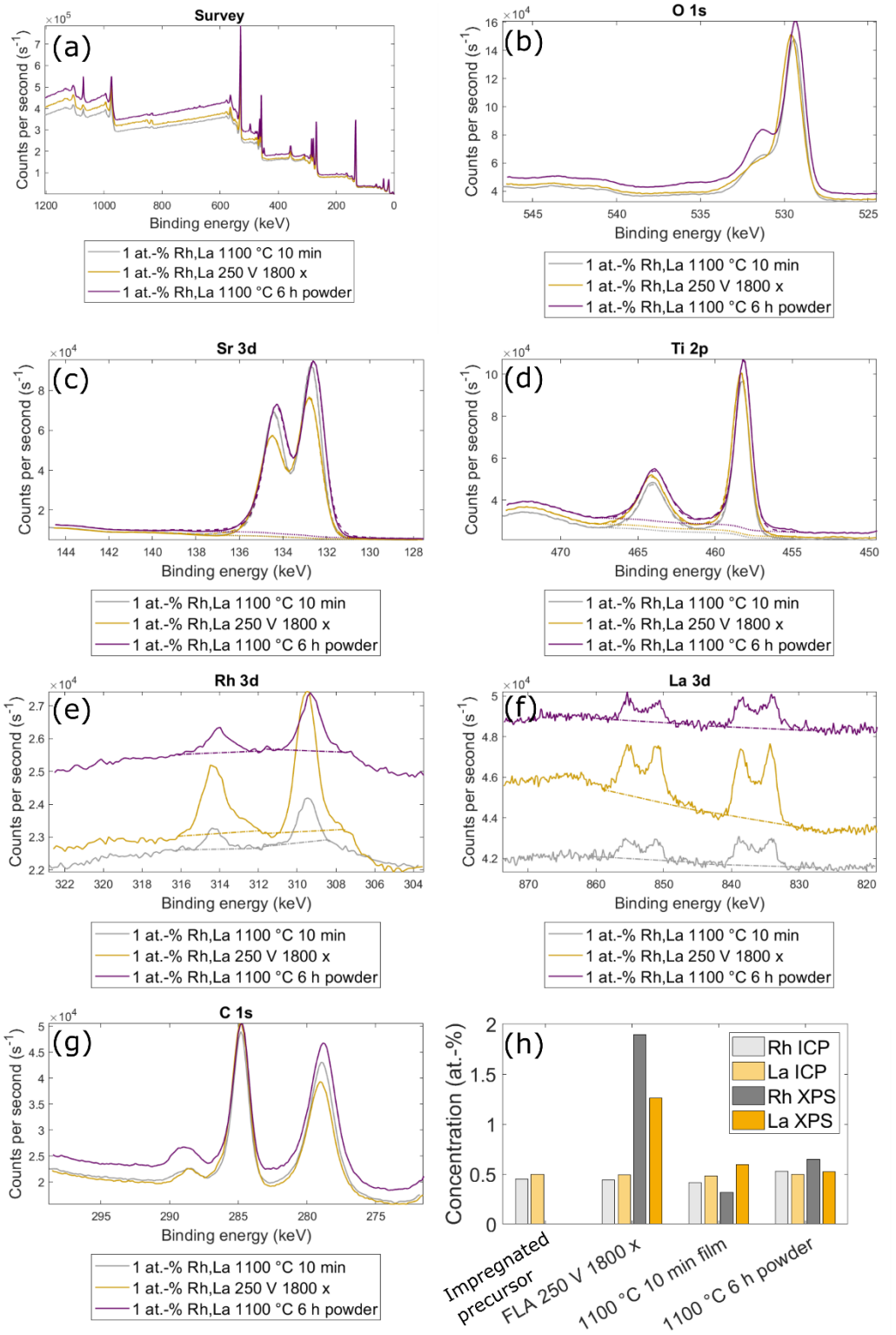

Figure S12: XPS spectra of 1 % Rh,La:$SrTiO_3$ from FLA and TA used for the quantification of the surface concentration of dopants in Figure 3a of the main text. (a) Survey spectrum, and high-resolution spectra of (b) O 1s, (c) Sr 3d, (d) Ti 2p, (e) Rh 3d, (f) La 3d, and (g) C 1s are shown. The background (··) and fitted envelope (--) used for quantification are added for Sr, Ti, Rh, and La. Due to the low concentration of dopants and issues with partial charging, the Rh oxidation state was not analyzed. (h) Quantification results for a 2nd data set on the same samples confirm similar trends as in Figure 3 (a) of the main text, but the Rh-La-ratios after FLA vary. Thus, they most likely result from measurement errors.

DLS particle size distributions

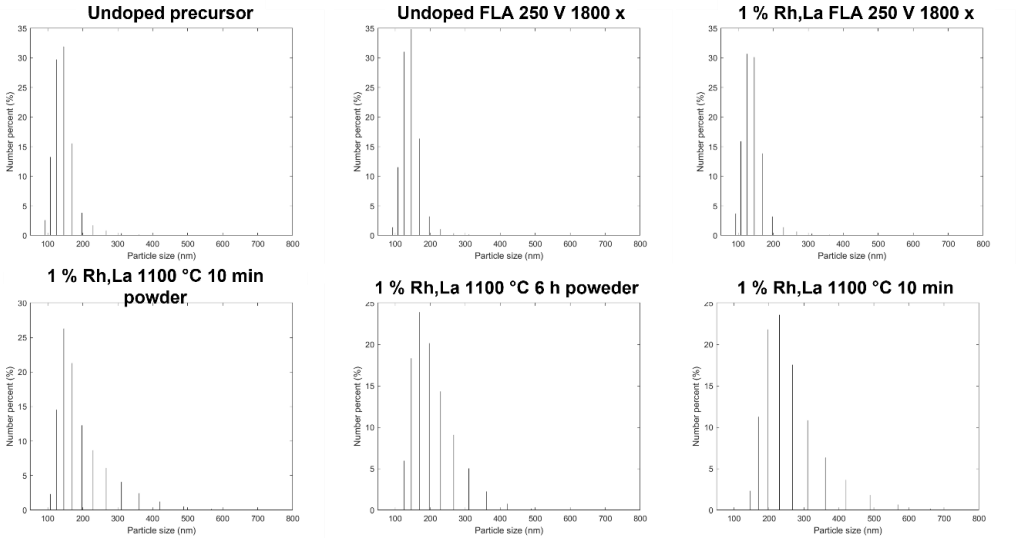

Figure S13: Particle size distributions as measured by DLS for undoped and doped samples prepared with FLA and TA.

Particle size analysis from STEM images

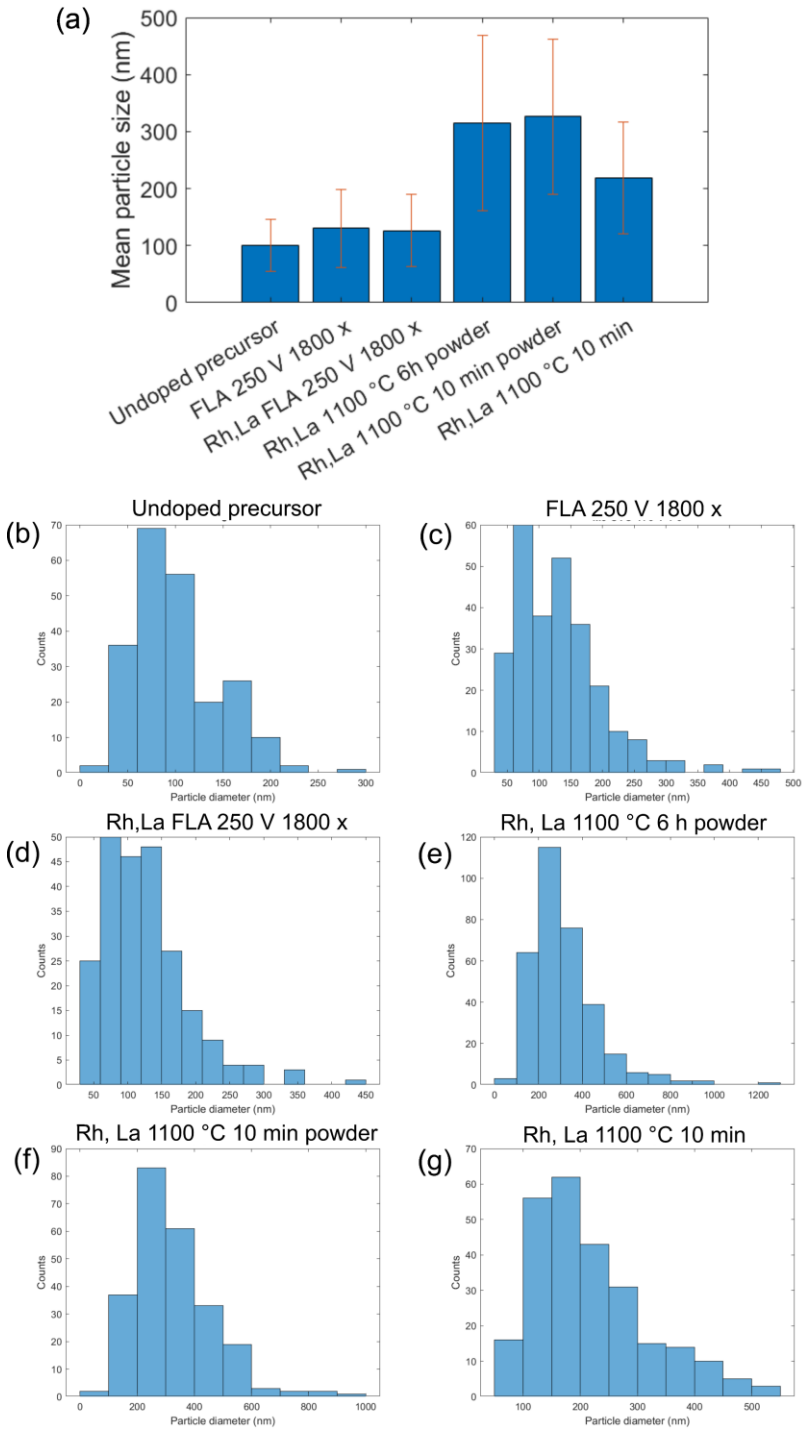

Figure S14: (a) Mean particle sizes and standard deviations for different samples obtained from the particle size distributions in (b) to (g). The higher difference between the precursor and FLA samples vs. TA samples based on TEM than DLS likely originates from the different counting method. In STEM images, all individual particles with no visible sloid connections to other particles through sintering were counted separately. Sintered particles were counted as one particle along their longest dimension. In contrast, DLS is based on particle dispersions, that may contain agglomerates of different sizes.

Photocatalytic performance data used for calculation of the apparent quantum yield (AQY)

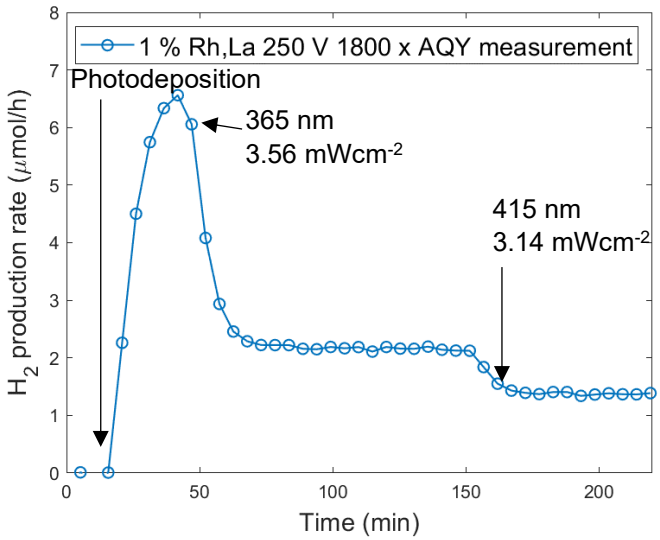

Figure S15: Raw data of H_2 production rate over the measurement time used for the calculations of the AQY (1 % Rh,La FLA 250 V 1800 x batch 2). Measurement conditions: 0.25 mg mL^{-1} in 40 mL of 0.2 M ascorbic acid solution with 0.4 wt.% Pt co-catalyst deposited by in-situ photodeposition, spot diameter 1.96 cm for 365 nm and 1.73 cm for 415 nm LED in top-illumination.

Additional thermal reference samples

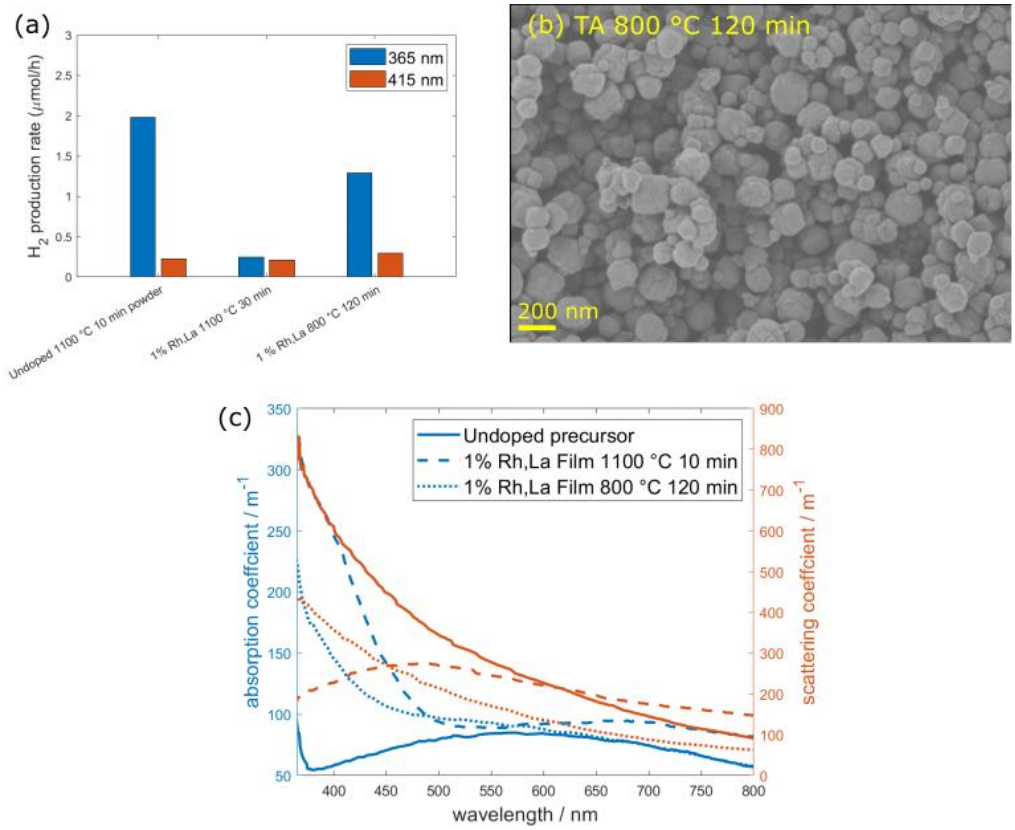

Figure S16: (a) Additional photocatalytic test results of undoped and 1 % Rh,La-doped samples from TA. Doping was not completed at 800 °C and 120 min. (b) The SEM image of the sample annealed at 800 °C and 120 min shows that restructuring of the surface was not completed. (c) Optical properties of samples annealed with TA at 1100 °C for 10 min and 800 °C for 120 min compared to the undoped precursor. The increase in visible light absorption is lower after annealing at 800 °C for 120 min.

Light spectra for photocatalytic testing

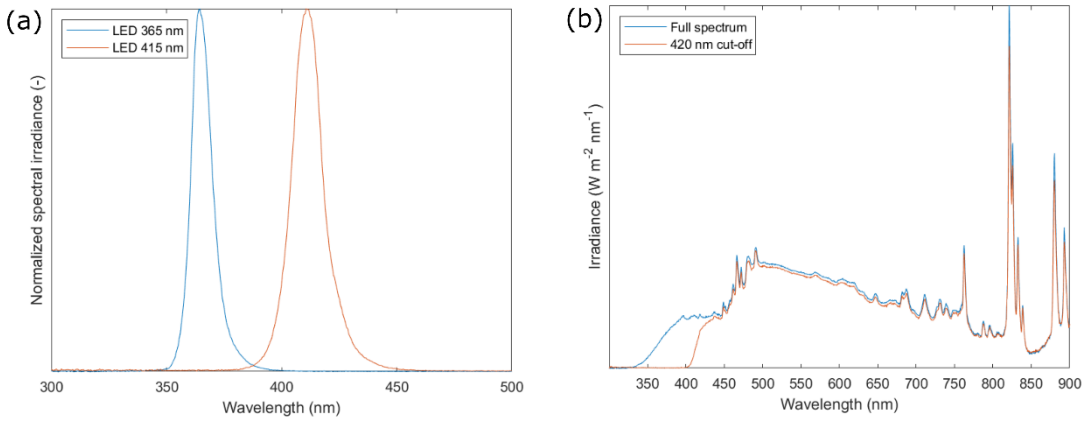

Figure S17: (a) LED emission spectra of the 365 and 415 nm LED used for photocatalytic performance tests. (b) Spectral shape for emission of the 450 W Xenon arc-lamp with KG 2 filter with and without the 420 nm cut-off filter used for photocatalytic tests under simulated sunlight.

TEM analysis of the sample crystallinity

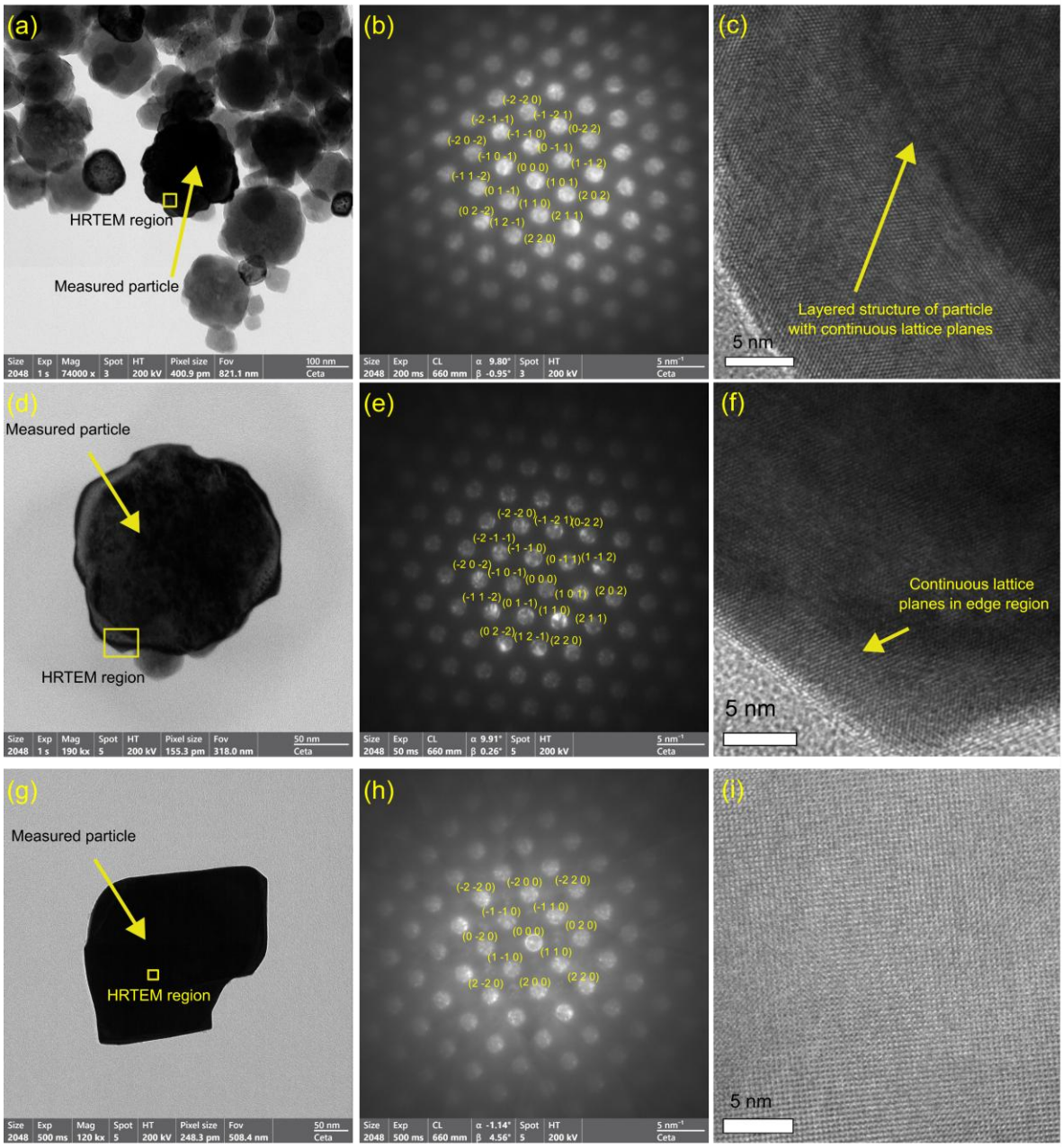

Figure S18: Brightfield TEM images of particles oriented to one zone axis, indexed convergent-beam electron diffraction (CBED) patterns, and HRTEM images of the regions highlighted in the TEM images for (a-c) the undoped $SrTiO_3$ precursor, (d-f) Rh,La:$SrTiO_3$ doped via FLA at 250 V and 1800 pulses, and (g-i) Rh,La:$SrTiO_3$ doped via TA at 1100 °C for 6 h as powder. The patterns in (b) and (e) match with cubic $SrTiO_3$ oriented along the [-111] zone axis while (h) is oriented along the [001] axis. The CBED patterns and HRTEM images show no indication for the presence of multiple crystallites within one particle The pristine precursor shows a distinct structure as a mesocrystal with parallel crystallographic alignment of smaller sub-particles (see c). The surface region of Rh,La:$SrTiO_3$ doped via FLA in (f) shows no distortions of the lattice planes on the doped surface. We therefore conclude that the precursor as well as samples doped via FLA and TA are single crystals and only the particle morphology evolves (see SEM images). This morphology change involves the fusion of sub-particles in the mesocrystal precursor.

Sr/Ti-ratios extracted from XPS data

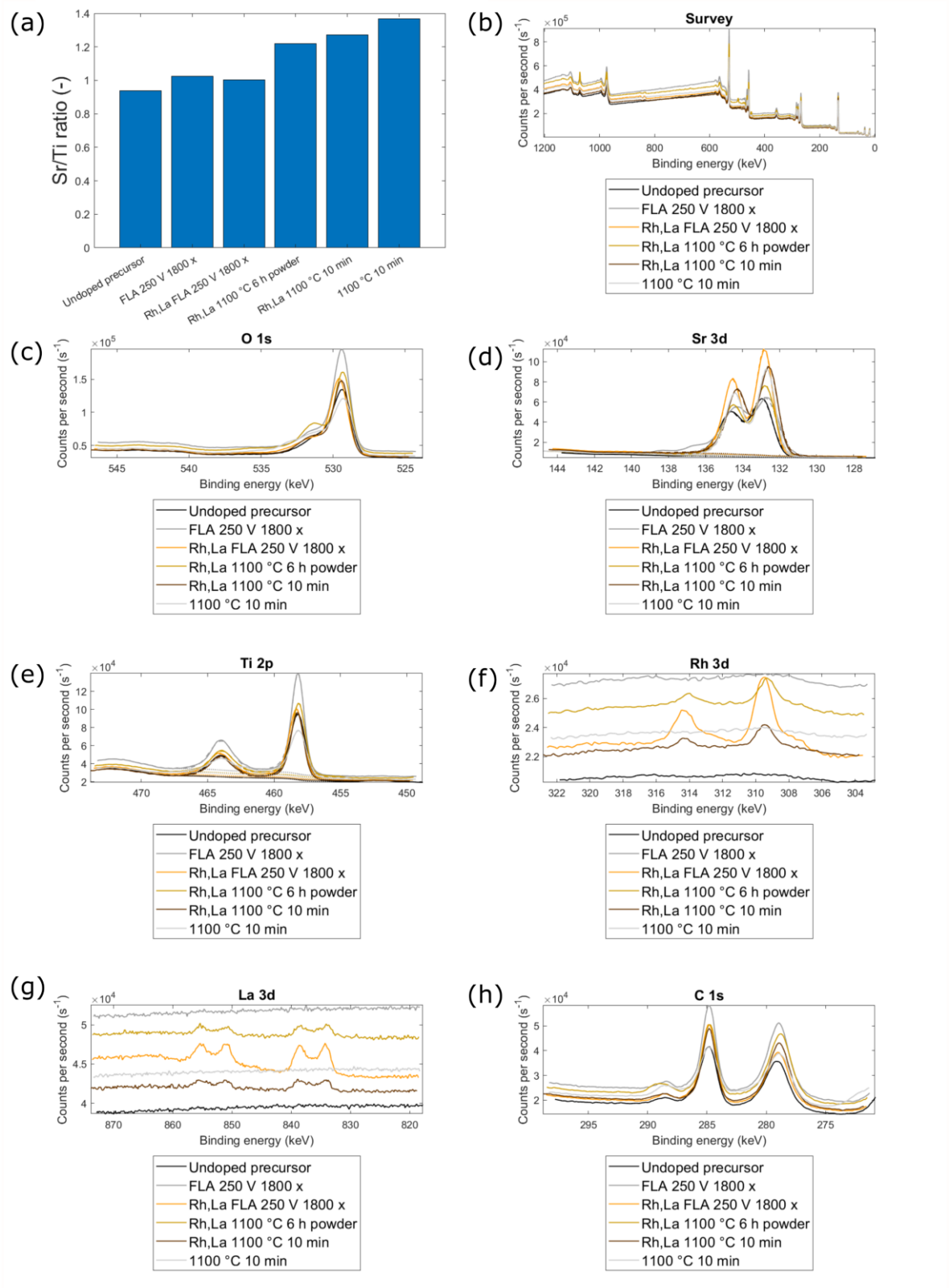

Figure S19: (a) Sr/Ti-ratios extracted from XPS data in (b-h) on the undoped precursor as well as undoped $SrTiO_3$ and Rh,La:$SrTiO_3$ samples prepared by FLA and TA. The background (··) and fitted envelope (--) used for quantification are added for Sr and Ti.

Reproducibility of FLA

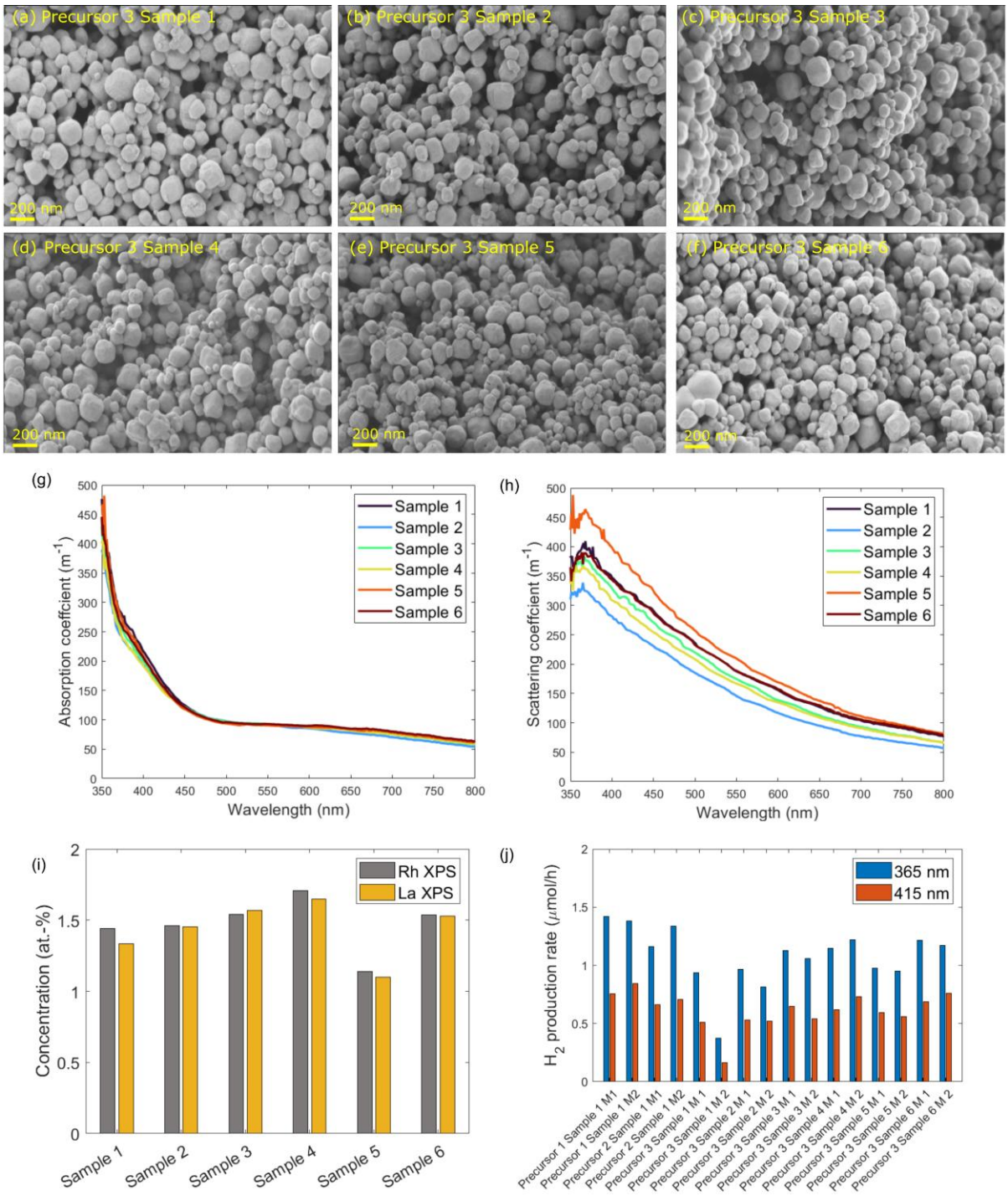

Figure S20: (a-f) SEM images of six different samples of Rh,La:$SrTiO_3$ obtained from the same precursor powder (precursor 3) and doped via FLA at 250 V and 1800 pulses. Optical (g) absorption and (h) scattering coefficients of the sample dispersions. (i) Surface dopant concentrations of the samples measured by XPS. (j) Photocatalytic performance of all six samples from precursor 3 and samples obtained from two other precursors 1 and 2. All samples were measured twice (M1 and M2). All performance data in the main text without the index "M1" and "M2" are mean values of at least two measurements on the same sample.

Influence of the substrate – Silicon compared to Al_2O_3 and quartz

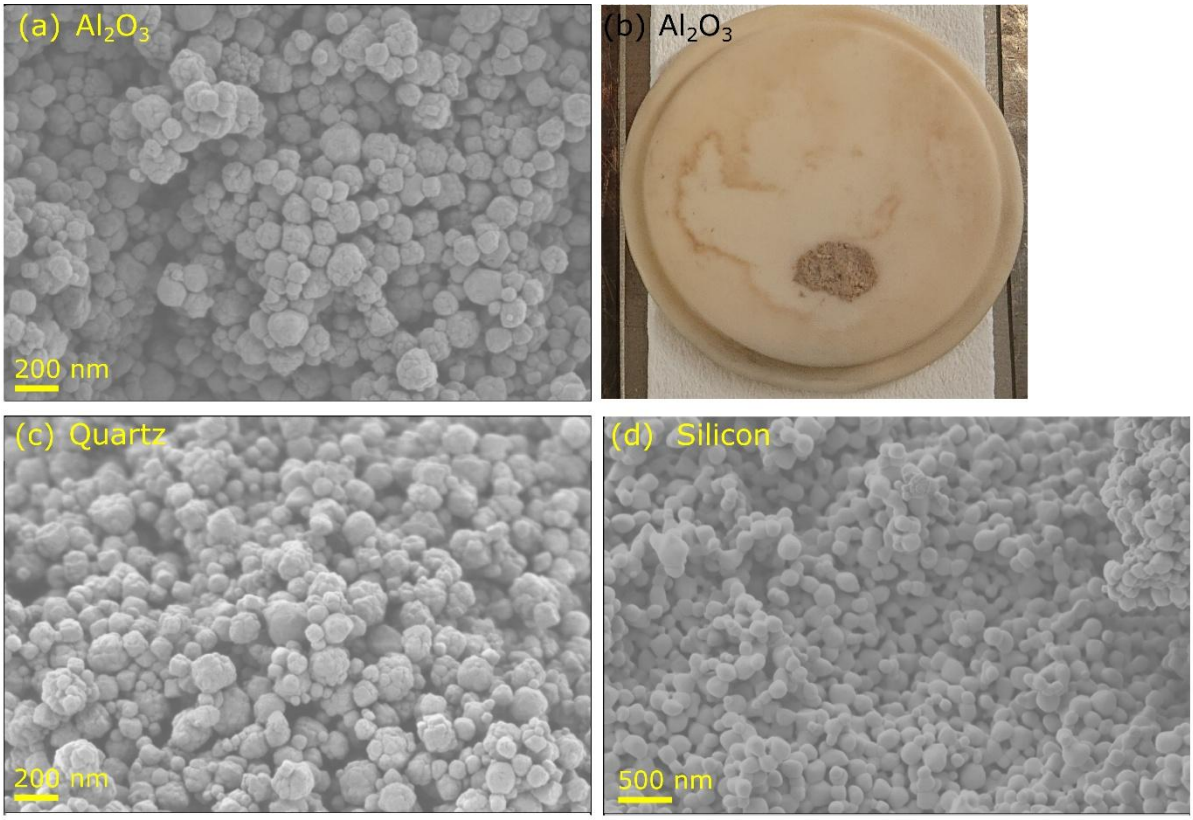

Figure S21: (a) SEM image and (b) photograph of 1 % Rh,La:$SrTiO_3$ powder after FLA (250 V, 1800 x) on an Al_2O_3 crucible lid and SEM images after FLA on (c) quartz and (d) a silicon wafer. Only the surface of powder annealed on silicon restructured.

Hydrothermal cubes FLA

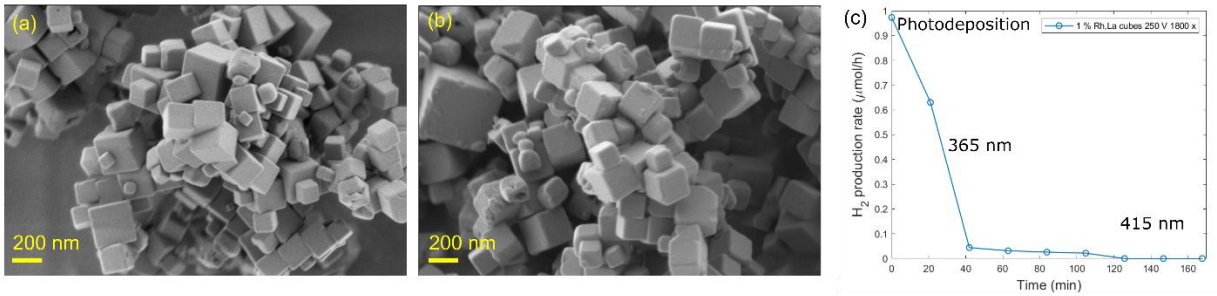

Figure S22: SEM images of the (a) undoped faceted $SrTiO_3$ cubes and (b) 1 % Rh,La-impregnated $SrTiO_3$cubes after FLA at 250 V and 1800 pulses. There is no significant change in the powder morphology. (c) Photocatalytic performance data of 1 % Rh,La:$SrTiO_3$ hydrothermal cubes after FLA at 250 V and 1800 pulses. The sample showed only negligible H_2 evolution.

Optical properties for variation of flash parameters

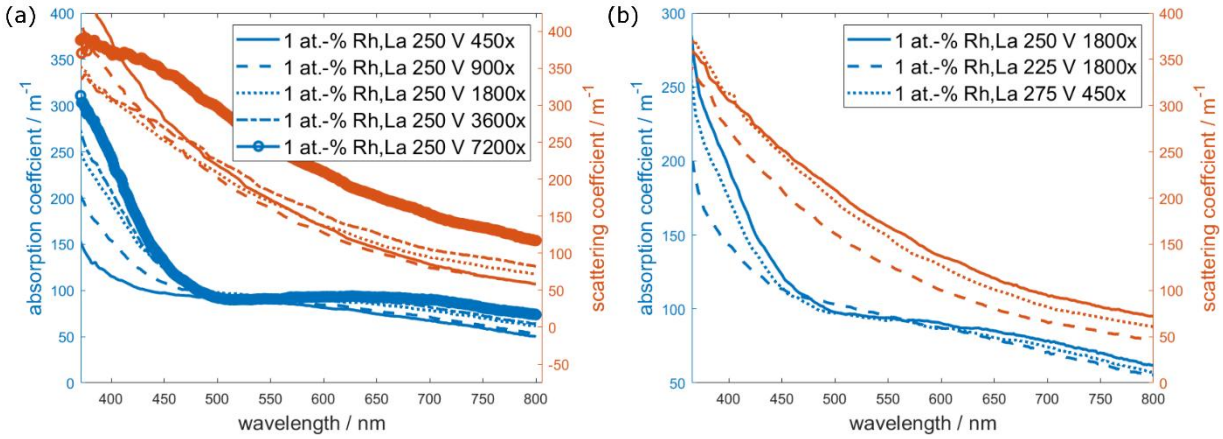

Figure S23: Optical absorption and scattering coefficients of dispersions (0.5 mgmL^{-1}) for 1 % Rh,La:$SrTiO_3$ FLA samples flashed (a) at 250 V for different number of pulses and (b) different voltages for 1800 or 450 pulses.

Change of morphology with FLA parameters

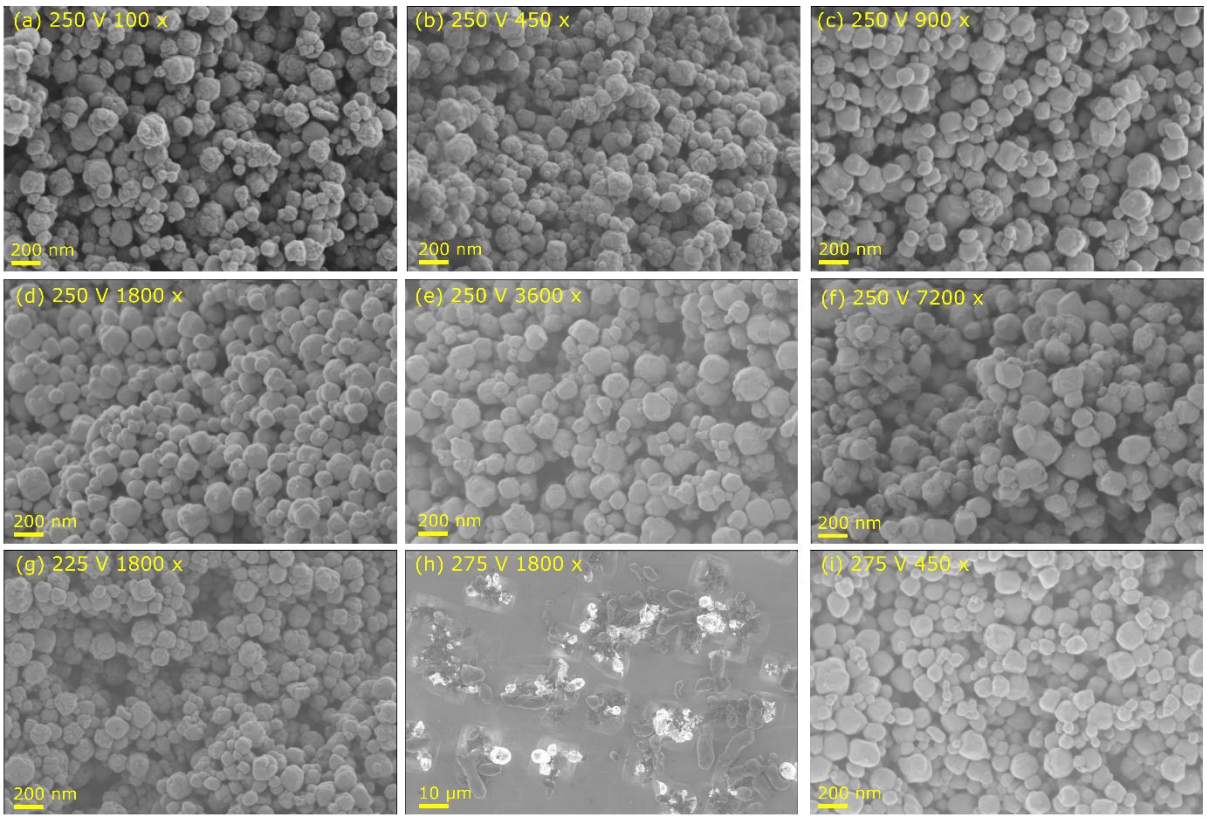

Figure S24: (a-f) SEM images for 1 % Rh,La:$SrTiO_3$ annealed with FLA at 250 V for different number of pulses. The images show a continuous evolution of the morphology with an initial surface restructuring followed by sintering. (g-h) SEM images for 1 % Rh,La:$SrTiO_3$ annealed with FLA at 225 and 275 V. The silicon wafer melted during flashing at 275 V for 1800 pulses, but doping was successful after 450 pulses at 275 V.

Simplified scheme of temperature profile and process control

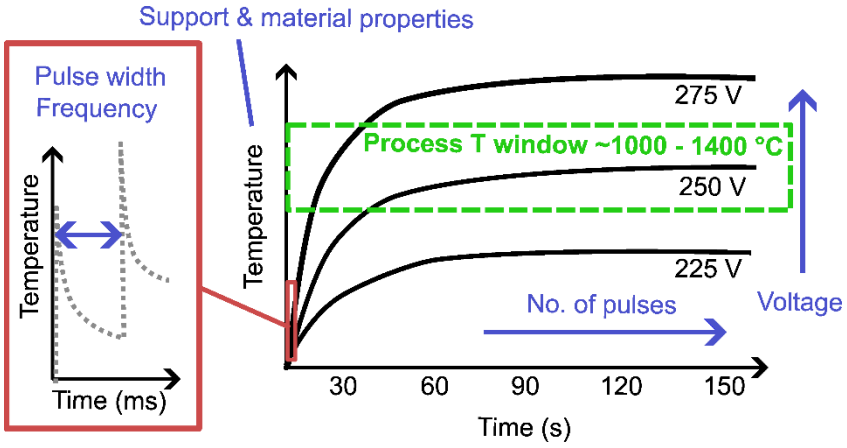

Figure S25: Proposed scheme for process control. On the second-scale, the energy balance depends on the lamp voltage and determines the equilibrium temperature reached during FLA. The number of pulses controls the annealing time after the equilibrium is established. On the millisecond-scale, the real temperature may exceed the overall equilibrium temperature depending on the location and time by an unknown amount due to illumination with pulsed light of high energy intensity. The optical and thermal properties of the material and support allow for additional process control.

Section 3: Supplementary tables

Table S1: Overview of flash-light annealing (FLA) conditions along with the calculated lamp power and total energy consumption per condition. A frequency of 60 Hz and pulse width of 1.5 ms were used for all FLA experiments. The energy consumption of the lamp was calculated based on the "Hereaus Noblelight technical reference book for arc and flash lamps".[1]

Voltage (V)	Number of pulses	Annealing duration (s)	Peak pulse power (kW)	Average power (kW)	Total energy consumption (kJ)
225	1800	30	59.2	5.3	159.9
250	450	7.5	81.2	7.3	54.8
250	900	15	81.2	7.3	109.7
250	1800	30	81.2	7.3	219.3
250	3600	60	81.2	7.3	438.6
250	7200	120	81.2	7.3	877.2
275	450	7.5	108.1	9.7	73.0
275	1800	30	108.1	9.7	291.9

ICP-MS elemental analysis

Table S2: ICP-MS results for doped and undoped samples after FLA and TA as well as the impregnated precursor. Silicon was not detectable in any of the tested samples. The dopant concentrations [Rh] Doping and [La] Doping are calculated as used for the nominal dopant concentration. Due to the Sr excess, the La concentration was calculated with respect to Ti as well as Sr. The concentrations [Rh] all and [La] all were calculated with respect to all four elements (Sr, Ti, Rh, and La) and used for the comparison to concentrations obtained from XPS. (loq: limit of quantification)

	Ti	Sr	Ti/Sr	Rh	[Rh] Doping	La	[La] Doping	Rh/La	[La] Doping	[Rh] all	[La] all	Si
Sample	**mmol/l**	**mmol/l**		**mmol/l**	**Rh/(Rh+Ti)**	**mmol/l**	**La/(La+Ti)**	**Rh/La**	**La/(La+Sr)**	**Rh/(Rh+ La+Sr+Ti)**	**La/(Rh+La+Sr+Ti)**	
Precursor 1 % Rh,La	1.92	2.09	0.92	0.018	0.94%	0.020	1.03%	0.904	0.95%	0.45%	0.50%	<loq
1 % Rh,La 1100 °C 6 h powder	2.49	2.68	0.93	0.028	1.10%	0.026	1.03%	1.074	0.96%	0.53%	0.50%	<loq
1 % Rh,La 1100 °C 10 min powder	1.27	1.37	0.93	0.011	0.89%	0.013	1.01%	0.879	0.93%	0.43%	0.48%	<loq
1 % Rh,La 1100 °C 10 min	1.36	1.49	0.91	0.012	0.87%	0.014	1.01%	0.867	0.92%	0.42%	0.48%	<loq
1 % Rh,La 250 V 1800 x	1.40	1.49	0.94	0.013	0.90%	0.014	1.02%	0.890	0.96%	0.44%	0.49%	<loq
Undoped 250 V 1800 x	1.97	2.17	0.91	<loq	N/A	<loq	N/A	N/A	N/A	N/A	N/A	<loq
Undoped 1100 °C 10 min	1.78	1.83	0.98	<loq	N/A	<loq	N/A	N/A	N/A	N/A	N/A	<loq

Section 4: References

(1) Heraeus. The Lamp Book - The Heraeus Noblelight Technical Reference Book for Arc and Flash Lamps. https://www-eng.lbl.gov/~shuman/NEXT/MATERIALS&COMPONENTS/Quartz/Hereaeus_LampBook_final_lowres.pdf (accessed 2025-07-09).

(2) Wang, Q.; Hisatomi, T.; Ma, S. S. K.; Li, Y.; Domen, K. Core/Shell Structured La- and Rh-Codoped $SrTiO_3$ as a Hydrogen Evolution Photocatalyst in Z-Scheme Overall Water Splitting under Visible Light Irradiation. *Chem. Mater.* **2014**, *26* (14), 4144–4150. https://doi.org/10.1021/cm5011983.

(3) Mu, L.; Zhao, Y.; Li, A.; Wang, S.; Wang, Z.; Yang, J.; Wang, Y.; Liu, T.; Chen, R.; Zhu, J.; Fan, F.; Li, R.; Li, C. Enhancing Charge Separation on High Symmetry $SrTiO_3$ Exposed with Anisotropic Facets for Photocatalytic Water Splitting. *Energy Environ. Sci.* **2016**, *9* (7), 2463–2469. https://doi.org/10.1039/C6EE00526H.

(4) Boga, B.; Steinfeldt, N.; Moustakas, N. G.; Peppel, T.; Lund, H.; Rabeah, J.; Pap, Z.; Cristea, V.-M.; Strunk, J. Role of SrCO3 on Photocatalytic Performance of SrTiO3-SrCO3 Composites. *Catalysts* **2022**, *12* (9), 978. https://doi.org/10.3390/catal12090978.

(5) Vaitkus, A.; Merkys, A.; Sander, T.; Quirós, M.; Thiessen, P. A.; Bolton, E. E.; Gražulis, S. A Workflow for Deriving Chemical Entities from Crystallographic Data and Its Application to the Crystallography Open Database. *J. Cheminformatics* **2023**, *15* (1), 123. https://doi.org/10.1186/s13321-023-00780-2.

(6) Merkys, A.; Vaitkus, A.; Grybauskas, A.; Konovalovas, A.; Quirós, M.; Gražulis, S. Graph Isomorphism-Based Algorithm for Cross-Checking Chemical and Crystallographic Descriptions. *J. Cheminformatics* **2023**, *15* (1), 25. https://doi.org/10.1186/s13321-023-00692-1.

(7) Vaitkus, A.; Merkys, A.; Gražulis, S. Validation of the Crystallography Open Database Using the Crystallographic Information Framework. *J. Appl. Crystallogr.* **2021**, *54* (2), 661–672. https://doi.org/10.1107/S1600576720016532.

(8) Quirós, M.; Gražulis, S.; Girdzijauskaitė, S.; Merkys, A.; Vaitkus, A. Using SMILES Strings for the Description of Chemical Connectivity in the Crystallography Open Database. *J. Cheminformatics* **2018**, *10* (1), 23. https://doi.org/10.1186/s13321-018-0279-6.

(9) Merkys, A.; Vaitkus, A.; Butkus, J.; Okulič-Kazarinas, M.; Kairys, V.; Gražulis, S. COD::CIF::Parser: An Error-Correcting CIF Parser for the Perl Language. *J. Appl. Crystallogr.* **2016**, *49* (1), 292–301. https://doi.org/10.1107/S1600576715022396.

(10) Gražulis, S.; Merkys, A.; Vaitkus, A.; Okulič-Kazarinas, M. Computing Stoichiometric Molecular Composition from Crystal Structures. *J. Appl. Crystallogr.* **2015**, *48* (1), 85–91. https://doi.org/10.1107/S1600576714025904.

(11) Gražulis, S.; Daškevič, A.; Merkys, A.; Chateigner, D.; Lutterotti, L.; Quirós, M.; Serebryanaya, N. R.; Moeck, P.; Downs, R. T.; Le Bail, A. Crystallography Open Database (COD): An Open-Access Collection of Crystal Structures and Platform for World-Wide Collaboration. *Nucleic Acids Res.* **2012**, *40* (D1), D420–D427. https://doi.org/10.1093/nar/gkr900.

(12) Gražulis, S.; Chateigner, D.; Downs, R. T.; Yokochi, A. F. T.; Quirós, M.; Lutterotti, L.; Manakova, E.; Butkus, J.; Moeck, P.; Le Bail, A. Crystallography Open Database – an Open-Access Collection of Crystal Structures. *J. Appl. Crystallogr.* **2009**, *42* (4), 726–729. https://doi.org/10.1107/S0021889809016690.

(13) Downs, R. T.; Hall-Wallace, M. The American Mineralogist Crystal Structure Database. *Am. Mineral.* **2003**, *88*, 247–250.

(14) Klinger, M. More Features, More Tools, More *CrysTBox*. *J. Appl. Crystallogr.* **2017**, *50* (4), 1226–1234. https://doi.org/10.1107/S1600576717006793.

(15) Klinger, M.; Jäger, A. *Crystallographic Tool Box* (*CrysTBox*): Automated Tools for Transmission Electron Microscopists and Crystallographers. *J. Appl. Crystallogr.* **2015**, *48* (6), 2012–2018. https://doi.org/10.1107/S1600576715017252.

(16) Klinger, M. *CrysTBox - Crystallographic Toolbox*; Institute of Physics of the Czech Academy of Sciences: Prague, 2015.

(17) Kant, P.; Trinkies, L. L.; Gensior, N.; Fischer, D.; Rubin, M.; Alan Ozin, G.; Dittmeyer, R. Isophotonic Reactor for the Precise Determination of Quantum Yields in Gas, Liquid, and Multi-Phase Photoreactions. *Chem. Eng. J.* **2023**, *452*, 139204. https://doi.org/10.1016/j.cej.2022.139204.
(18) Kant, P. *phoRex & QY photoreactor - Monte Carlo ray tracing in MATLAB® & quantum yield measurements*. https://doi.org/10.5445/IR/1000150817.
(19) Kant, P. P. *Optimierung von Fotokatalysatoren und Fotoreaktoren für die Synthese solarer Kraftstoffe = Optimizing photocatalysts and photoreactors for solar fuel synthesis*. https://doi.org/10.5445/IR/1000162170.
(20) Khashan, M. A.; Nassif, A. Y. Dispersion of the Optical Constants of Quartz and Polymethyl Methacrylate Glasses in a Wide Spectral Range: 0.2–3 Mm. *Opt. Commun.* **2001**, *188* (1), 129–139. https://doi.org/10.1016/S0030-4018(00)01152-4.
(21) Hale, G. M.; Querry, M. R. Optical Constants of Water in the 200-Nm to 200-Mm Wavelength Region. *Appl. Opt.* **1973**, *12* (3), 555–563. https://doi.org/10.1364/AO.12.000555.
(22) Patiny, L. Unlocking the Potential of Browser- Based Scientific Data Analysis: A 20-Year Journey of Expertise. *CHIMIA* **2025**, *79* (1–2), 66–69. https://doi.org/10.2533/chimia.2025.66.
(23) Jablonka, K. M.; Patiny, L.; Smit, B. Making the Collective Knowledge of Chemistry Open and Machine Actionable. *Nat. Chem.* **2022**, *14* (4), 365–376. https://doi.org/10.1038/s41557-022-00910-7.